SPANDIDOS PUBLICATIONS

MOLECULAR MEDICINE REPORTS 28: 236, 2023

Ferroptosis contributes to hemolytic hyperbilirubinemia-induced brain damage *in vivo* and *in vitro*

JINFU ZHOU[1,2*], XINPEI LIN[1,3*], SINING LIAO[1,3], GUILIN LI[1,3], JIANPING TANG[1,3], JINYING LUO[4], CHENRAN ZHANG[1,3], SIYING WU[3,5,6], LIANGPU XU[2] and HUANGYUAN LI[1,3,5]

[1]Department of Preventive Medicine, School of Public Health, Fujian Medical University, Fuzhou, Fujian 350122; [2]Department of Medical Genetic Diagnosis and Therapy Center, Fujian Maternity and Child Health Hospital, College of Clinical Medicine for Obstetrics & Gynecology and Pediatrics, Fujian Medical University, Fuzhou, Fujian 350001; [3]Fujian Provincial Key Laboratory of Environmental Factors and Cancer, School of Public Health, Fujian Medical University, Fuzhou, Fujian 350122; [4]Department of Obstetrics and Gynecology, Fujian Maternity and Child Health Hospital, College of Clinical Medicine for Obstetrics & Gynecology and Pediatrics, Fujian Medical University, Fuzhou, Fujian 350001; [5]The Key Laboratory of Environment and Health; [6]Department of Epidemiology and Health Statistics, School of Public Health, Fujian Medical University, Fuzhou, Fujian 350122, P.R. China

Received May 15, 2023; Accepted September 19, 2023

DOI: 10.3892/mmr.2023.13123

Abstract. Ferroptosis is driven by iron-dependent accumulation of lipid hydroperoxides, and hemolytic hyperbilirubinemia causes accumulation of unconjugated bilirubin and iron. The present study aimed to assess the role of ferroptosis in hemolytic hyperbilirubinemia-induced brain damage (HHIBD). Rats were randomly divided into the control, phenylhydrazine (PHZ) and deferoxamine (DFO) + PHZ groups, with 12 rats in each group. Ferroptosis-associated biochemical and protein indicators were measured in the brain tissue of rats. We also performed tandem mass tag-labeled proteomic analysis. The levels of iron and malondialdehyde were significantly higher and levels of glutathione (GSH) and superoxide dismutase activity significantly lower in the brain tissues of the PHZ group compared with those in the control group. HHIBD also resulted in significant increases in the expression of the ferroptosis-related proteins acyl-CoA synthetase long-chain family member 4, ferritin heavy chain 1 and transferrin receptor and divalent metal transporter 1, as well as a significant reduction in the expression of ferroptosis suppressor protein 1. Kyoto Encyclopedia of Genes and Genomes pathway enrichment analysis demonstrated that the differentially expressed proteins of rat brain tissues between the control and PHZ groups were significantly involved in ferroptosis, GSH metabolism and fatty acid biosynthesis pathways. Pretreatment with DFO induced antioxidant activity and alleviated lipid peroxidation-mediated HHIBD. In addition, PC12 cells treated with ferric ammonium citrate showed shrinking mitochondria, high mitochondrial membrane density, and increased lipid reactive oxygen species and intracellular ferrous iron, which were antagonized by pretreatment with ferrostatin-1 or DFO, which was reversed by pretreatment with ferrostatin-1 or DFO. The present study demonstrated that ferroptosis is involved in HHIBD and provided novel insights into candidate proteins that are potentially involved in ferroptosis in the brain during hemolytic hyperbilirubinemia.

Correspondence to: Professor Huangyuan Li, The Key Laboratory of Environment and Health, School of Public Health, Fujian Medical University, 1 Xuefu North Road, Fuzhou, Fujian 350122, P.R. China
E-mail: fmulhy@163.com

Dr Liangpu Xu, Department of Medical Genetic Diagnosis and Therapy Center, Fujian Maternity and Child Health Hospital, College of Clinical Medicine for Obstetrics & Gynecology and Pediatrics, Fujian Medical University, 18 Daoshan Road, Gulou, Fuzhou, Fujian 350001, P.R. China
E-mail: xiliangpu@fjmu.edu.cn

[*]Contributed equally

Key words: neonatal hemolytic hyperbilirubinemia, brain damage, ferroptosis, iron overload, lipid peroxidation

Introduction

Hyperbilirubinemia, one of the most common disorders in newborns, is characterized by an imbalance between bilirubin production and elimination (1). Aberrant accumulation of bilirubin may cause bilirubin encephalopathy, which is the most serious complication of neonatal hyperbilirubinemia that can lead to neonatal death (2-4). Survivors often have neurological sequelae, including learning disabilities, movement disorders, mental retardation and cerebral palsy (5). Neonatal bilirubin encephalopathy causes 4.8% of all pediatric hospitalization and its mortality is estimated to be 16.1% in a multicenter study in China (6). Although a number of treatment options have been employed for the treatment of neonatal hyperbilirubinemia, including phototherapy and

exchange transfusion (7), neurological damage may still occur, suggesting that several other factors contribute to increased neurotoxicity (8). Hemolysis and its major byproduct, ferrous ion (Fe^{2+}), are among the factors that serve important roles in the development of neurotoxicity (9,10); however, the underlying mechanism remains unclear.

In both developing and developed countries, hemolysis is one of the risks factors for hyperbilirubinemia (11). During excessive hemolysis, increased amounts of iron are released from damaged red blood cells. Iron enters the endothelial cells that form the blood-brain barrier via transferrin receptor-mediated endocytosis, or it is independently transported as non-protein-bound iron (12). A significant increase in non-protein-bound iron levels and an imbalance between pro-oxidant and antioxidant systems is observed in neonatal hemolytic diseases (10,13).

Ferroptosis, a recently identified form of programmed cell death that differs from apoptosis and necrosis, is driven by iron-dependent accumulation of lipid hydroperoxides (14). Dysregulation of iron homeostasis, glutathione (GSH) depletion and lipid peroxidation are closely linked to cell sensitivity to ferroptosis (15). Iron homeostasis imbalance has been implicated in ferroptosis, which may lead to pathological conditions in the central nervous system (16,17). Studies have reported that ferroptosis is involved in numerous neurodegenerative diseases, such as Alzheimer's disease (16,18), Parkinson's disease (19), ischemic stroke (20), intracerebral hemorrhage (21) and traumatic brain injury (22). These conditions lead to increased hemoglobin release and iron overload, resulting in an abnormal increase in lipid peroxidation, which is the main cause of secondary injury and neuronal ferroptosis (23). Hemolytic hyperbilirubinemia also results in an increased release of hemoglobin and iron (11).

Moreover, specific features of ferroptosis, such as increased products of lipid peroxidation, are similar to those that appear in iron-mediated neurological dysfunction caused by neonatal hemolytic diseases (24). In a rat model of hemolytic hyperbilirubinemia-induced brain damage (HHIBD), comparing to the control group, the level of malondialdehyde (MDA) increased and GSH decreased in brain tissues of the treatment group, closely resembling the biochemical characteristics of ferroptosis (25,26). It is therefore hypothesized that ferroptosis may contribute to the pathogenesis of neuronal dysfunction induced by neonatal hemolytic hyperbilirubinemia (8). However, the contribution of ferroptosis to hemolytic HHIBD remains unclear. The present study, utilizing both *in vitro* and *in vivo* assays, assessed the role of ferroptosis in HHIBD.

Materials and methods

Modeling neonatal hemolytic hyperbilirubinemia in rats. A total of 60 male Sprague-Dawley (SD) rats (aged 10-12 days; 24-28 g) were purchased from the Laboratory Animal Center, Fujian Medical University (Fuzhou, China). Rat pups were housed in the same standard laboratory polycarbonate cage with their mothers at a suitable temperature (21±2˚C) and humidity (50±10%) with 12/12-h light/dark cycles to maintain their circadian rhythm. Maternal milk was used to feed the rat pups, while adult female rats had free access to standardized granular food (Beijing Keao Xieli Feed Co., Ltd.) and tap water. The 10-12 day old rat pups were randomly divided into the control, phenylhydrazine (PHZ) and deferoxamine (DFO) + PHZ groups, with 12 rats in each group.

To establish bilirubin encephalopathy secondary to hemolysis, 75 mg/kg PHZ (Sigma-Aldrich; Merck KGaA) was injected intraperitoneally once daily for 2 days, based on previous reports (26,27). Rats in the DFO + PHZ group were injected intraperitoneally with DFO (100 mg/kg; cat. no. D9533; Sigma-Aldrich; Merck KGaA) 1 h prior to administration of PHZ (28,29) whilst rats in the PHZ group received the same volume of saline. Control rats received the same volume of saline in parallel. Subsequently, 24 h after the last dosing, all animals were anesthetized intraperitoneally with 100 mg/kg pentobarbital sodium and then euthanized by decapitation to collect trunk blood and brain tissue. A total of 0.5 ml blood from each rat was collected and centrifuged at 1,500 x g at 4˚C for 10 min and then preserved at -80˚C for later biochemical analysis. Brain tissue was immediately collected, placed in liquid nitrogen for 5 min, and then stored at -80˚C for future analysis. All treatments were performed with care and rat suffering was minimized. During the experiment, none of the rats reached any of the following humane endpoints: Inability to drink the maternal milk, labored breathing, inability to stand or no response to external stimuli. Death was verified by monitoring the cessation of breathing and heartbeat and pupil dilation. No animals were found dead before the end of the experiment.

Cell culture and drug treatment. The highly differentiated PC12 cell line, derived from a pheochromocytoma of the rat adrenal medulla, resembles neurons and is widely used in the study of neurological diseases *in vitro* (30,31). PC12 cells (Wuhan Boster Biological Technology, Ltd.) were cultured in Dulbecco's Modified Eagle Medium (cat. no. C11995500BT; Gibco; Thermo Fisher Scientific, Inc.), supplemented with 10% fetal bovine serum (cat. no. SV30207.03; HyClone; Cytiva) and 100 U/ml penicillin-streptomycin (cat. no. V900929; Sigma-Aldrich; Merck KGaA). Cells were cultured at 37˚C as monolayers in a humidified atmosphere containing 5% CO_2. Based on MTT cell viability assay results (Fig. S1) and the level of superoxide dismutase (SOD), MDA and reactive oxygen species (ROS) in the PC12 cells exposed to 0, 200 and 400 μM ferric ammonium citrate (FAC; cat. no. F5879; Sigma-Aldrich; Merck KGaA) for 24 h (Fig. S2), 400 μM FAC treatment for 24 h was selected for subsequent experiments, to assess the mechanism of iron overload-induced neurotoxicity *in vitro*. PC12 cells were pretreated with 10 μM ferrostatin-1 (Fer-1; cat. no. SML0583; Sigma-Aldrich; Merck KGaA) or 100 μM DFO for 1 h at 37˚C and exposed to 400 μM FAC.

Measurement of serum hemoglobin, hematocrit and bilirubin levels. Serum hemoglobin and hematocrit levels were assessed using an automated analyzer (Coulter LH 780; Beckman Coulter, Inc.). Another automated analyzer (Architect ci16200 Integrated System; Abbott Pharmaceutical Co. Ltd.) was used to measure the serum levels of total bilirubin, indirect bilirubin and direct bilirubin using a diazo reagent-based method (32). All procedures strictly followed the manufacturers' instructions.

Measurement of S100 calcium-binding protein B (S100B) and serum neuron-specific enolase (NSE) levels. Serum levels of S100B were assessed using the Rat S100B ELISA kit (cat. no. E-EL-R0868; Elabscience Biotechnology, Inc.), and those of serum NSE were assessed using the Rat NSE ELISA Kit (cat. no. E-EL-R0058c; Elabscience Biotechnology, Inc.) according to the manufacturer's instructions.

Measurement of SOD activity, MDA and reduced GSH/oxidized glutathione disulfide (GSSG) levels. A total of 15 mg brain tissue from six rats in each group was placed into 200 μl ice-cold 10% radioimmunoprecipitation assay lysis buffer (RIPA; cat, no. P0013E; Beyotime Institute of Biotechnology). Brain samples were homogenized using a tissue homogenizer (cat. no. KZ-III-F; Wuhan Servicebio Technology Co., Ltd.) and centrifuged at 1,000 x g for 10 min at 4˚C. The supernatant was then transferred into microcentrifuge tubes. For cell extracts, PC12 cells were seeded in the 6-well plate at a density of 50-60% for 24 h, and then exposed to FAC . A total of 200 μl RIPA lysis buffer were added to plate to homogenize the sample and centrifuged at 1,000 x g for 10 min at 4˚C, waiting for next measurement.

SOD activity and total GSH/GSSG detection kits (cat. nos. A001-3-1 and A061-1-1; Nanjing Jiancheng Bioengineering Institute) were used to assess SOD and GSH/GSSG levels, respectively. Tissue iron detection kits (cat. no. A039-2-1; Nanjing Jiancheng Bioengineering Institute) were used to assess tissue iron levels. An MDA detection kit (cat. no. S0131S; Beyotime Institute of Biotechnology) was used to assess MDA levels. All assays were conducted in triplicate according to the manufacturers' protocols.

Kyoto Encyclopedia of Genes and Genomes (KEGG) enrichment analysis. Proteomic analysis of separate triplicate brain tissue samples from the control and PHZ groups was performed by tandem mass tag (TMT) labeling (Cat. no. A44520; Thermo Fisher) (33) and liquid chromatography-tandem mass spectrometry (Q Exactive™ HF-X; Thermo Fisher) (34). The detection was conducted by multiple reaction monitoring (MRM) in negative ionization mode. The electrospray voltage was 2.1 kV. The m/z scan range was 350-1600 for the full scan, and intact peptides at a resolution of 120,000 were detected in the Orbitrap. We set the automatic gain control (AGC) at 3E6, and the fixed first mass was 100 m/z. The nitrogen gas temperature was at 300˚C with a flow rate of 5 l/min and nebulizer pressure was 40 psi. The differentially abundant protein (DAP) screening parameters were adjusted to $P<0.05$ and $\log_2$ fold change=0, KEGG enrichment analysis was performed using ClueGO (v2.5.6; https://apps.cytoscape.org/apps/cluego) (35). The databases used were KEGG_20.05.2019 (genome.jp/kegg/pathway.html) and Gene Ontology (GO) (https://www.geneontology.org/)_ Biological Process-EBI-Uniprot-GO Annotation_20.05.2019 (https://david.ncifcrf.gov/home.jsp). The GO term 'fusion mode' was selected according to the P-value <0.05.

Protein-protein interaction network analysis. The number of differential protein sequences in the protein database (Maxquant: v1.6.15.0; https://www.maxquant.org/) screened according to a 1.2 expression difference multiplesin PHZ group vs. Control group, and then compared with those in the protein network interaction database of the Search Tool for the Retrieval of Interacting Genes/Proteins (STRING; v. 11.0; https://cn.string-db.org/), with a confidence score of >0.7 (high confidence). The differential protein interaction was analyzed, and the R package (Dev-version: 0.4; christophergandrud.github.io/networkD3/) 'networkD3' function was used to visually display the differential protein interaction network.

Cell viability assay. In the FAC model, PC12 cells were seeded in 96-well plates for 24 h at a density of $1x10^4$ cells/well. Cells were then treated with different concentrations of FAC (0, 100, 200, 400 and 800 μM, 1 and 5 mM) for 3, 6, 12 and 24 h. The viability of PC12 cells was assessed using MTT (cat. no. F5655; Sigma-Aldrich; Merck KGaA). Briefly, after the aforementioned treatments, MTT (5 mg/ml) was added to the 96-well plate. The plate was incubated at 37˚C for 4 h to allow the formazan crystals to form. The medium was then discarded and 100 μl dimethyl sulfoxide was added to dissolve the formazan. Absorbance was measured at a detection wavelength of 570 nm using a plate reader (Thermo Fisher Scientific, Inc.).

Measurement of lipid oxidation using confocal laser scanning microscopy. After PC12 cells were seeded in the 35 mm confocal dish (cat. no. FCFC016; Beyotime Institute of Biotechnology; China) at a density of 50 %, the cells were treated with FAC as aforementioned for 24 h, and then were rinsed with phosphate-buffered saline (PBS) three times. To visualize neuronal lipid oxidation, 10 μM BODIPY 581/591 C11 (cat. no. D3861; Thermo Fisher Scientific, Inc.) was added to each well and incubated at 37˚C for 0.5 h and stained with 1 μg/ml DAPI for 5 min at 37˚C. Cells were rinsed with PBS three times and imaged using a confocal laser scanning microscope (SP5; Leica Microsystems GmbH) (36). The argon laser (excitation, 488 nm; emission, 500-535 nm) was used to detect oxidized lipids, whereas the white light laser (excitation, 561 nm; emission, 573-613 nm) was used to detect non-oxidized lipids.

Measurement of ROS levels. PC12 cells were seeded in the 6-well plates for 24 h at a density of $2x10^5$ cells/well and then were treated with FAC for 24 h as aforementioned. Subsequently, cells were stained with the ROS indicator 2',7'-dichlorodihydrofluorescein diacetate (cat. no. S0033S; Beyotime Institute of Biotechnology) for 30 min at 37˚C. Subsequently, the cells were washed with PBS three times and digested with 0.25 % trypsin (cat. no. C0201S; Beyotime Institute of *Biotechnology*) at 37˚C for 2 min. Finally, labelled cells were detected with a flow cytometer (LSRFortessa™ X-20; BD Biosciences) and analyzed by Flow v10.9 (BD Biosciences) (37).

Detection of intracellular free iron using fluorescence microscopy. FerroOrange (cat. no. F374; Dojindo Laboratories, Inc.) was used to detect intracellular Fe^{2+}. PC12 cells were seeded in the 12-well plates for 24 h at a density of $2x10^5$ cells/well and then were treated with 400 μM FAC as aforementioned., They were rinsed with PBS and stained with 1 μM FerroOrange at 37˚C for 0.5 h. The cells were rinsed with PBS three times and imaged under a fluorescence microscope (38).

Transmission electron microscopy (TEM). PC12 cells were seeded in a 10 cm dish for 24 h at a density of $1x10^6$ cells/well and then exposed to FAC as aforementioned. Subsequently, cells were fixed in 2.5% glutaraldehyde (diluted in 0.1 μM PBS; pH 7.4) at 25˚C for 24 h and then post-fixed in 1% osmium tetroxide (dissolved in 0.1 μM PBS; pH 7.4) at 25˚C for 60 min. After dehydration with ethanol (50, 70, 80, 90 and 100%), samples were embedded by resin (cat. no. 45347; Merck) with different condition (37˚C for 12 h; 45˚C for 12 h; 60˚C for 12 h) and ultrathin sectioning (50 nm). Then, the samples were stained with uranyl acetate at room temperature for 30 min and stained with lead citrate at room temperature for 8 min. Digital images were captured using TEM (FEI Tecnai G2 F30; Thermo Fisher Scientific, Inc.) (39).

Western blotting. Proteins were extracted from brain tissue using RIPA lysis buffer (cat. no. P0013E; Beyotime Institute of Biotechnology) supplemented with phenylmethylsulfonyl fluoride and then denatured at 95˚C in 5X protein loading buffer (cat. no. P0286; Beyotime Institute of Biotechnology) for 10 min. The concentration of protein in sample were measured by Enhanced BCA Protein Assay Kit (cat. no. P0009; Beyotime Institute of Biotechnology) according to the manufacturer's instructions. An equal amount of protein samples (20 μg/lane) were added to per lane and then were separated on 10% gels by SDS-PAGE. Proteins were then transferred to 0.2 μm PVDF membranes and blocked with 5% non-fat milk for 60 min at room temperature. PVDF membranes were incubated overnight at 4˚C with primary antibodies against the following: Rabbit acyl-coenzyme A synthetase long-chain family member 4 (ACSL4; 1:1,000; cat. no. A16848; ABclonal Biotech Co., Ltd.); ferritin heavy chain (FTH; 1:1,000; cat. no. A19544; ABclonal Biotech Co., Ltd.); transferrin receptor 1 (TFRC; 1:1,000; cat. no. A5865; ABclonal Biotech Co., Ltd.); ferroportin 1 (FPN1; 1:1,000; cat. no. A14884; ABclonal Biotech Co., Ltd.); divalent metal transporter 1 (DMT1; 1:1,000; cat. no. A10231; ABclonal Biotech Co., Ltd.); iron regulatory protein 2 (IRP2; 1:1,000; cat. no. A6382; ABclonal Biotech Co., Ltd.); GAPDH (1:5,000; cat. no. A19056; ABclonal Biotech Co., Ltd.); xCT (1:1,000; cat. no. ab175186; Abcam); GSH peroxidase 4 (GPX4; 1:1,000; cat. no. ab125066; Abcam) and ferroptosis suppressor protein 1 (FSP1; 1:1,000; cat. no. AVARP09054_P050; Aviva Systems Biology, Corp). After washing by TBS buffer with 0.1% Tween-20 (cat. no. ST1727; Beyotime Institute of Biotechnology) , PVDF membranes were incubated with horseradish peroxidase-conjugated secondary antibodies (1:8,000; cat. no. 31460; Thermo Fisher) at 37˚C for 60 min. Enhanced chemiluminescence detection was performed (cat. no. 1705061; BIO-RAD) (40) and ImageJ software (version 1.53; National Institutes of Health) was used to semi-quantify the protein bands.

Statistical analysis. Data are presented as mean ± standard error of the mean. All analyses were conducted using GraphPad Prism 8.0 (GraphPad Software; Dotmatics). Significance of differences between two groups was analyzed using two-way independent-sample t-test. For three or more groups, one-way analysis of variance followed by Tukey's post-hoc test was used to determine significance. $P<0.05$ was considered to indicate a statistically significant difference.

Results

Successful establishment of the hemolytic hyperbilirubinemia model. To establish a hemolytic hyperbilirubinemia model of neonatal SD rats, PHZ was used to increase erythrocyte turnover via hemolysis (Fig. S3A). In the PHZ group, the appearance of the neonatal rats and their brains was more jaundiced than that of the control group (Fig. S3B and C). PHZ group had significantly decreased hematocrit and hemoglobin levels compared with the control group (Fig. S3D and E). Moreover, the serum levels of three types of bilirubin (total, direct and indirect bilirubin) significantly increased in the PHZ group compared with that of the control group (Fig. S3F-H), indicating that the hemolytic hyperbilirubinemia model was established successfully.

Subsequently, changes in the brain injury markers NSE and S100B in the PHZ group were assessed. Compared with those in the control group, serum S100B and NSE levels were significantly increased in the PHZ group (Fig. 1A and B). Simultaneously, the concentration of iron significantly increased in the brain tissue of the PHZ group compared with that of the control group (Fig. 1C). Disturbances in oxidative balance caused by hemolytic hyperbilirubinemia were then assessed. SOD, which serves an important function in the first line of antioxidant defense, significantly decreased in the brains of the PHZ group compared with that of the control group (Fig. 1G). Compared with the control group, the GSH and GSH/GSSG levels significantly decreased in the PHZ group. However, there was no difference in the level of GSSG between the two groups (Fig. 1D-F). Similarly, the level of lipid peroxidation, as assessed by detecting the levels of MDA, significantly increased in the PHZ group compared with that of the control group (Fig. 1H). Overall, these results suggested that hemolytic hyperbilirubinemia could disrupt the redox balance in rat brains, resulting in brain injury. However, the specific mechanism of action remained unclear. Therefore, mass spectrometry analysis was performed to evaluate the potential molecular mechanisms of hemolytic hyperbilirubinemia.

Ferroptosis participates in brain damage induced by hemolytic hyperbilirubinemia. Proteomic analysis of brain tissue samples from the control and PHZ groups were performed in triplicate using TMT labelling to evaluate whether ferroptosis is involved in HHIBD. KEGG analysis using ClueGO software demonstrated the enrichment of ferroptosis-related proteins in the PHZ group compared with those in the control group. When the DAPs screening parameters were adjusted to $P<0.05$ and $\log_2$ fold change=0, compared with the control, a total of 26 ferroptosis-associated DAPs were demonstrated to be enriched in the PHZ group (Fig. 2A). These DAPs were also involved in other metabolic pathways, including mineral absorption, glutathione metabolism, and fatty acid biosynthesis. The STRING database was then used to determine the protein-protein interaction network (Fig. 2B; confidence score >0.7) among the screened ferroptosis-associated DAPs.

To evaluate the hypothesis that ferroptosis has a role in HHIBD, ferroptosis-associated proteins were assessed using western blotting. As it was previously demonstrated that the iron concentration in the brain tissue of the PHZ group

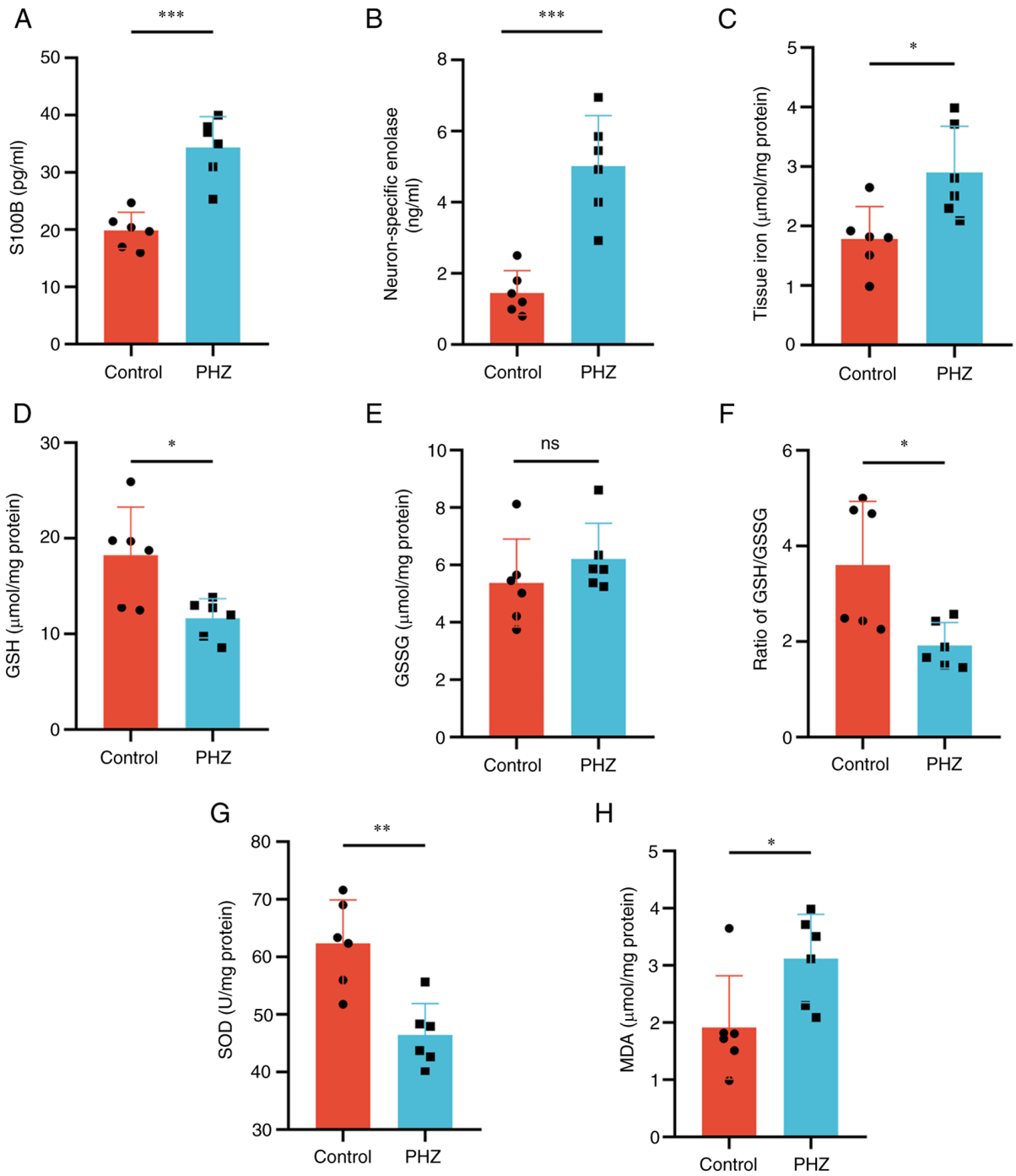

Figure 1. Hemolytic hyperbilirubinemia-induced brain damage in neonatal Sprague-Dawley rats. Serum levels of (A) S100B and (B) neuron-specific enolase. (C) Tissue iron levels in the brain. Redox imbalances assessed by measuring levels of (D) GSH, (E) GSSG, (F) GSH/GSSG, (G) SOD and (H) MDA. n=6. *P<0.05; **P<0.01; ***P<0.001. S100B, S100 calcium-binding protein B; GSH, glutathione; GSSG, glutathione disulfide; SOD, superoxide dismutase; MDA, malondialdehyde; PHZ, phenylhydrazine; ns, not significant.

significantly increased compared with that of the control group (Fig. 1C), protein-controlled iron import and export were assessed. The levels of the iron transporters TFRC (Fig. 3A and B) and DMT1 (Fig. 3A and C), which represent important components of ferroptosis that regulate iron levels, significantly increased in the PHZ group compared with that of the control group, whilst FPN1 levels did not significantly change (Fig. S4A and B). The results also demonstrated that levels of the iron storage protein FTH significantly increased in the PHZ group compared with that of the control group (Fig. 3D and F). Furthermore, the levels of IRP2, which is involved in the regulation of iron metabolism, significantly increased in the brain in the PHZ group compared with that of the control group (Fig. 3D and E). ACSL4 is a specific biomarker and driver of ferroptosis (41), while FSP1 has been identified as key molecules in independent pathways associated with ferroptosis inhibition (42). ACSL4 levels significantly increased and FSP1 levels significantly decreased in the PHZ group compared with that of the control group (Fig. 3G-I). The level of GPX4, an inhibitor of ferroptosis that converts

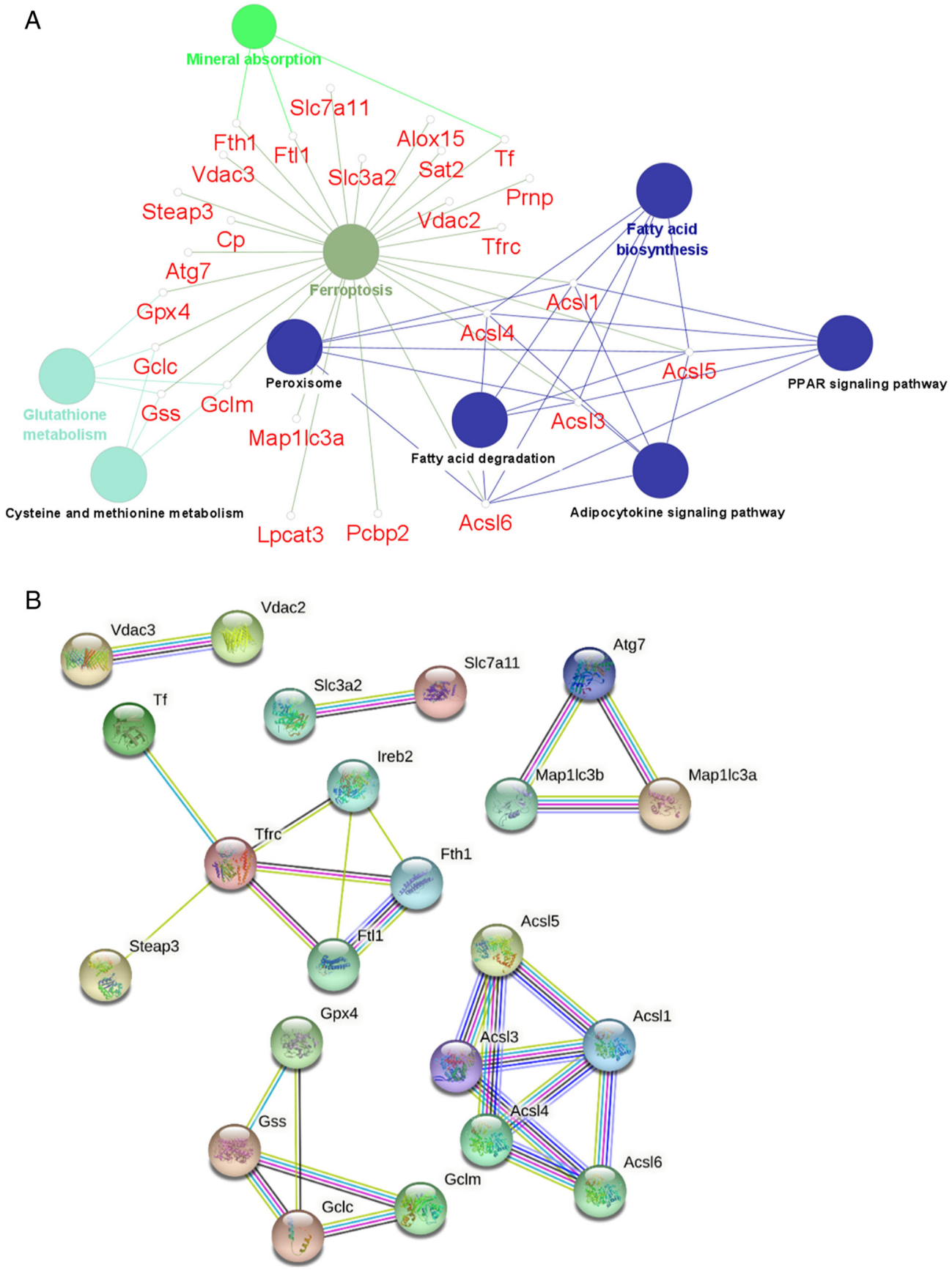

Figure 2. Kyoto Encyclopedia of Genes and Genomes pathway and PPI network analysis of differentially abundant proteins enriched in ferroptosis (A) Kyoto Encyclopedia of Genes and Genomes pathway analysis of differentially abundant proteins using ClueGO software. (B) PPI network analysis associated with hemolytic hyperbilirubinemia-induced brain damage. Search Tool for the Retrieval of Interacting Genes/Proteins 11.0 database was used for PPI analysis with a confidence score of >0.7 (high confidence). The network nodes correspond to interacting proteins and the edges represent the predicted functional associations. Each of the colored lines represents different evidence for each interaction: Red, gene fusions; green, gene neighborhood; blue, gene co-occurrence; purple, experimentally determined; yellow, text mining; light blue, from curated databases. PPI, protein-protein interaction.

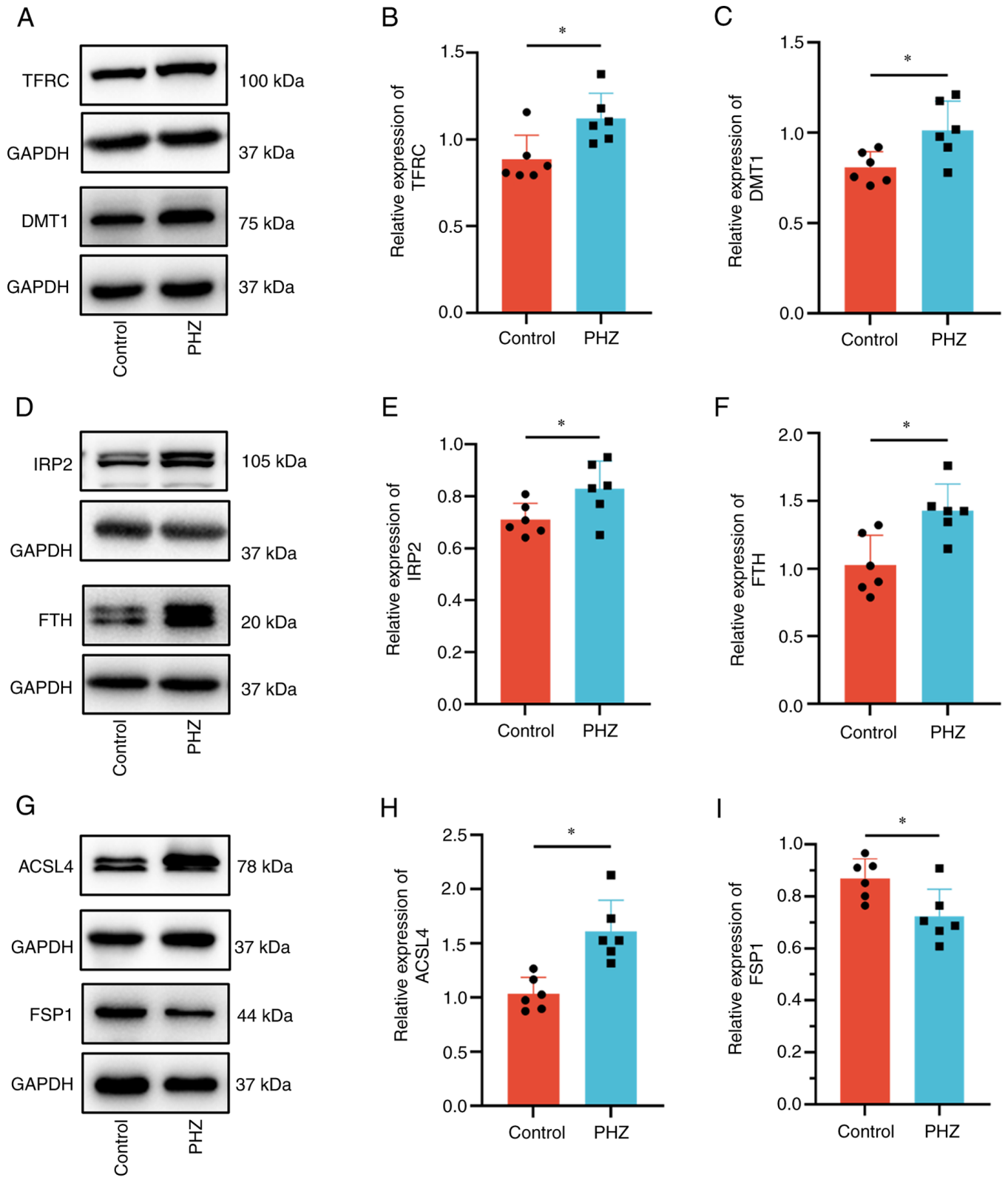

Figure 3. Changes in the expression of ferroptosis-associated proteins in the brain following treatment with PHZ. (A) Expression levels of TFRC and DMT1 determined using western blotting and semi-quantitative analysis of the protein expression of (B) TFRC and (C) DMT1. (D) Expression levels of IRP2 and FTH determined using western blotting and semi-quantitative analysis of the protein expression of (E) IRP2 and (F) FTH. (G) Expression levels of ACSL4 and FSP1 determined using western blotting and semi-quantitative analysis of the protein expression of (H) ACSL4 and (I) FSP1. n=6. *P<0.05. PHZ, phenylhydrazine; TFRC, transferrin receptor 1; DMT1, divalent metal transporter 1; IRP2, iron regulatory protein 2; FTH, ferritin heavy chain; ACSL4, acyl-coenzyme A synthetase long-chain family member 4; FSP1, ferroptosis suppressor protein 1.

lipid hydroperoxides into non-toxic lipid alcohols, was also demonstrated to have significantly increased after the onset of hemolytic hyperbilirubinemia in the PHZ group compared with that of the control group (Fig. S4A and C). By contrast,

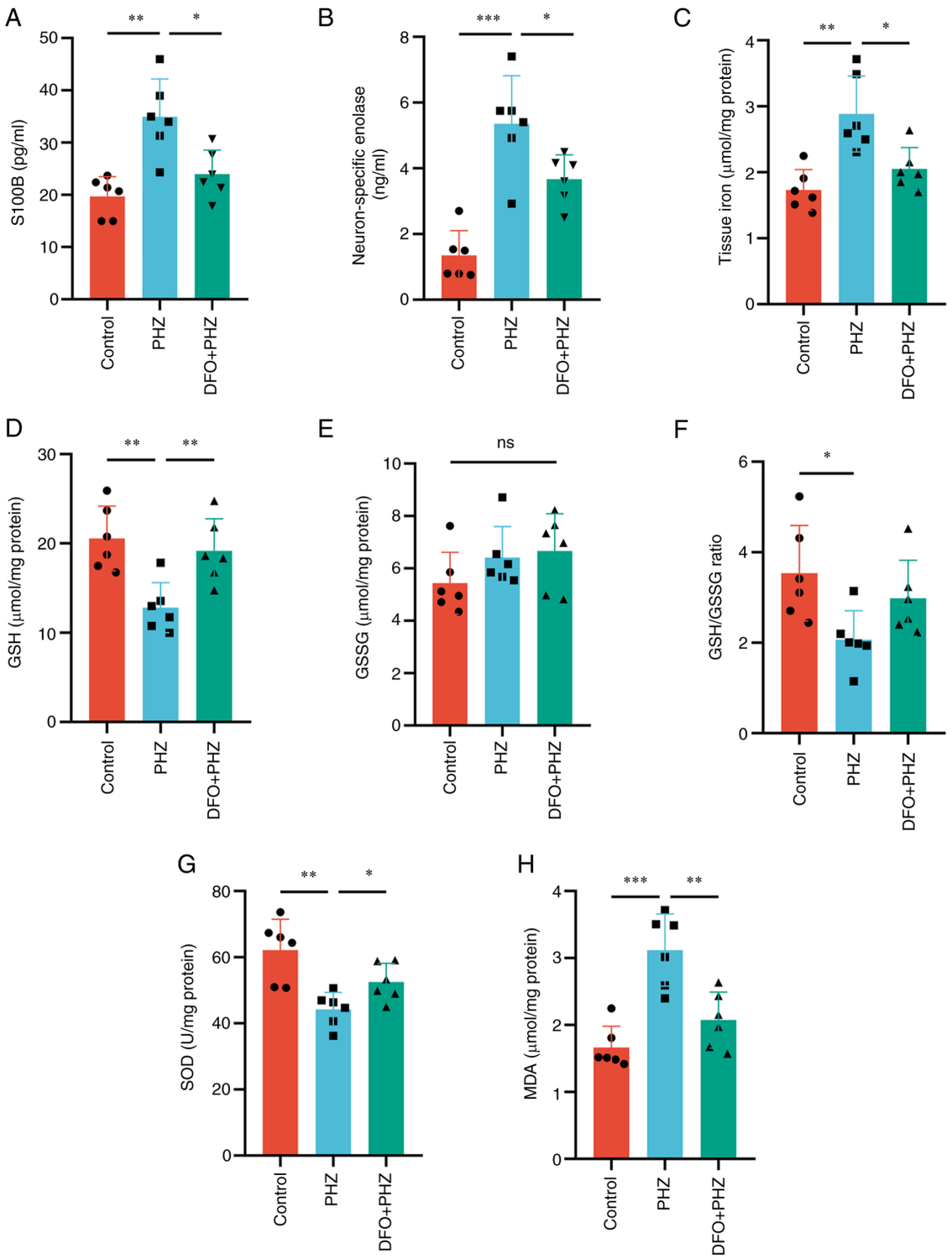

Figure 4. DFO pretreatment alleviates hemolytic hyperbilirubinemia-induced brain damage in neonatal Sprague-Dawley rats. Serum levels of (A) S100B and (B) neuron-specific enolase. (C) Levels of iron in the brain. Redox imbalances assessed by measuring the levels of (D) GSH, (E) GSSG, (F) GSH/GSSG, (G) SOD and (H) MDA. n=6. *P<0.05; **P<0.01; ***P<0.001. DFO, deferoxamine; S100B, S100 calcium-binding protein B; GSH, glutathione; GSSG, glutathione disulfide; SOD, superoxide dismutase; MDA, malondialdehyde; PHZ, phenylhydrazine; ns, not significant.

the level of xCT, an important antioxidant defense molecule, did not change significantly (Fig. S4A and D).

Effect of the neuroprotective ferroptosis inhibitor DFO on HHIBD. DFO and its function as an iron chelator and specific inhibitor of ferroptosis (28,29), was used to further assess the function of ferroptosis in HHIBD. Compared with that in the PHZ group, DFO did not significantly influence the levels of hematocrit, hemoglobin and bilirubin in the DFO + PHZ group (Fig. S5). However, DFO pretreatment significantly reduced the levels of NSE and S100B, compared with that of the PHZ only group, indicating that brain injury was alleviated (Fig. 4A and B). DFO mitigated the imbalanced iron levels in the brain (Fig. 4C), thereby partially alleviating the

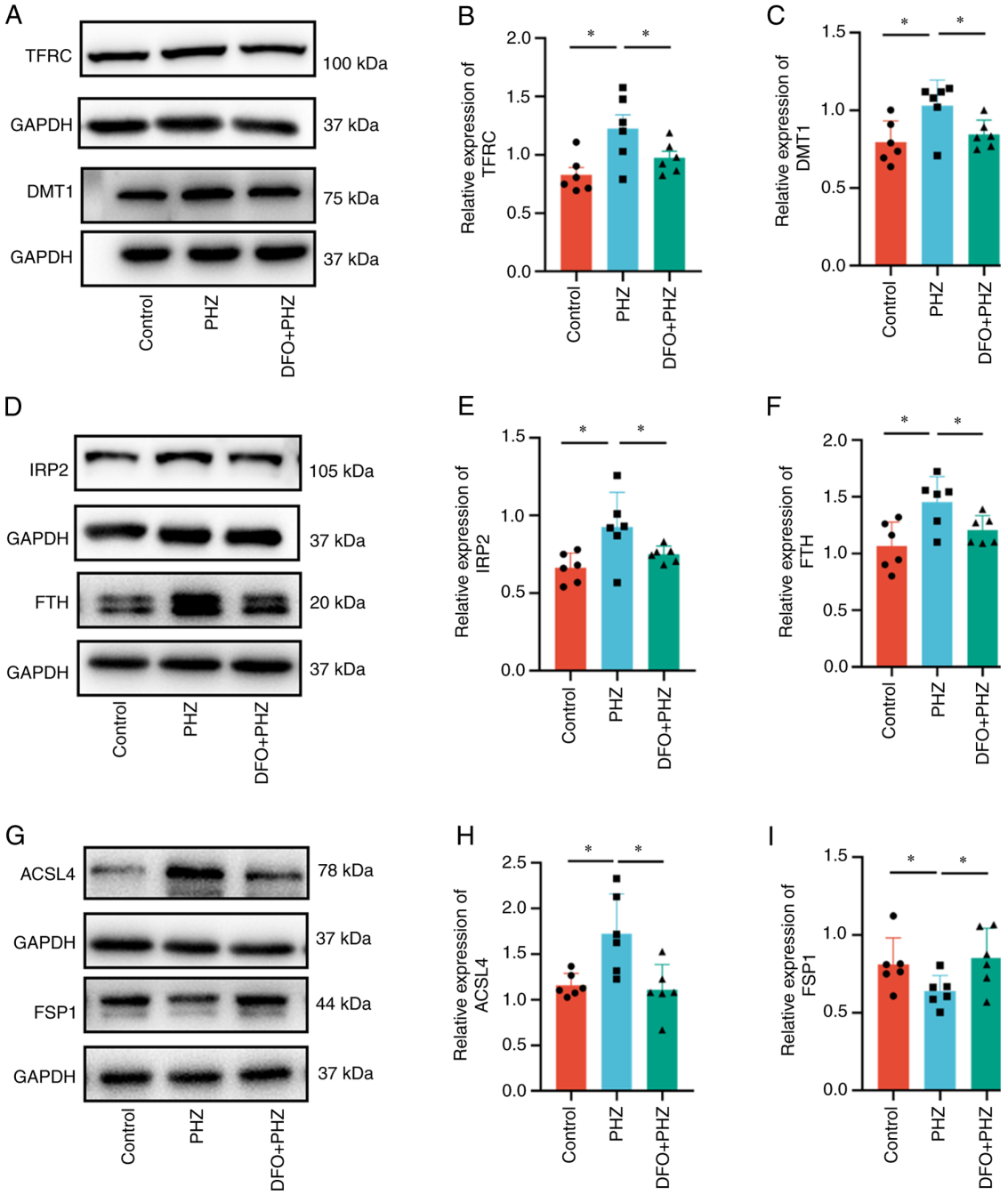

Figure 5. Ferroptosis is mitigated in neonatal Sprague-Dawley rats following DFO pretreatment. (A) Protein expression levels of TFRC and DMT1 determined using western blotting and semi-quantitative analysis of the protein expression of (B) TFRC and (C) DMT1. (D) Protein expression levels of IRP2 and FTH determined using western blotting and semi-quantitative analysis of protein expression of (E) IRP2 and (F) FTH. (G) Protein expression levels of ACSL4 and FSP1 determined using western blotting and semi-quantitative analysis of the protein expression of (H) ACSL4 and (I) FSP1. n=6. *P<0.05. DFO, deferoxamine; TFRC, transferrin receptor 1; DMT1, divalent metal transporter 1; IRP2, iron regulatory protein 2; FTH, ferritin heavy chain; ACSL4, acyl-coenzyme A synthetase long-chain family member 4; FSP1, ferroptosis suppressor protein 1; PHZ, phenylhydrazine.

redox imbalance compared with the PHZ group. The levels of GSH and SOD were increased following treatment with DFO (Fig. 4D-G), whereas MDA levels were significantly reduced, compared with that of the PHZ only group (Fig. 4H). There was no difference in the level of GSSG between the DFO + PHZ groups and the PHZ group (Fig. 4E).

The effect of DFO on the proteins related to ferroptosis was then evaluated. The protein levels of DMT1 and TFRC, which regulate iron transport in and out of cells, were decreased following DFO treatment compared with those of the PHZ group (Fig. 5A-C), whereas the FPN1 level was not significantly altered (Fig. S6A and B). Similarly, DFO restored the levels of IRP2 and FTH proteins compared with those of the PHZ group (Fig. 5D-F). Moreover, the altered levels of the key proteins in the ferroptosis pathway, ACSL4 and FSP1, were decreased following DFO treatment (Fig. 5G-I). However, the protein level of xCT did not significantly change following DFO pretreatment (Fig. S6A and D). Furthermore, compared with the PHZ group, the GPX4 level decreased in the DFO + PHZ group (Fig. S6A and C).

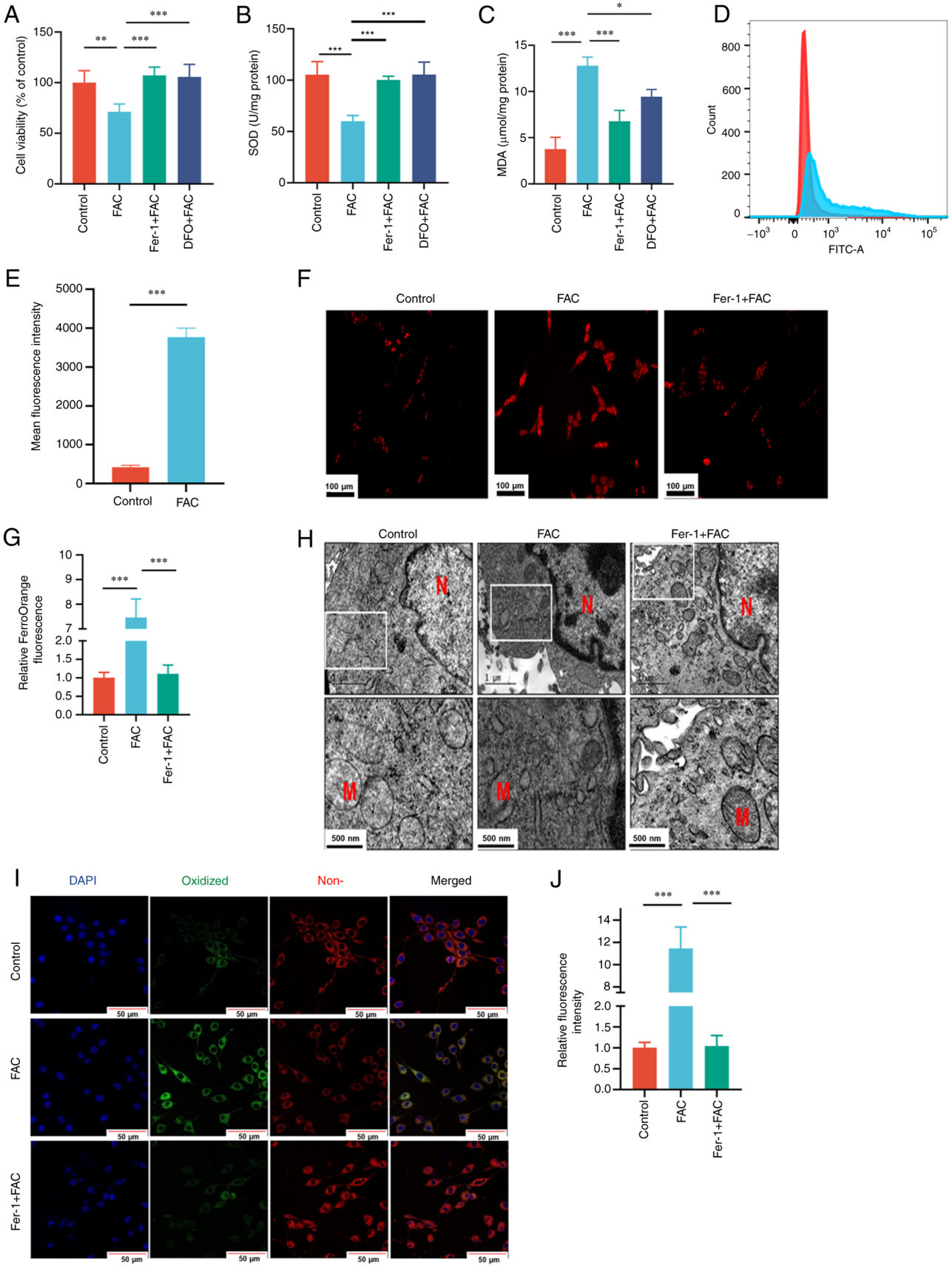

Figure 6. PC12 cells were pretreated with 100 μM DFO or 10 μM Fer-1 for 1 h and then exposed to 400 μM FAC for 24 h. (A) Cell viability was assessed using an MTT assay. Level of (B) SOD activity and (C) MDA in PC12 cells. (D) Level of reactive oxygen species in PC12 cells assessed using 2',7'-dichlorodihydrofluorescein diacetate via flow cytometry and (E) quantified. (F) Concentrations of free iron assessed using FerroOrange staining (scale bar, 100 μm). (G) Relative FerroOrange fluorescence. (H) Mitochondrial morphology observed using transmission electron microscopy (scale bar, 1 μm, upper images; 500 nm, lower images). (I) Confocal microscopy images of the oxidized and non-oxidized variants of lipid peroxides stained using a BODIPY C11 probe (scale bar, 50 μm). (J) Relative fluorescence intensity of oxidized variants of lipid peroxides. n=3. *P<0.05; **P<0.01; ***P<0.001. DFO, deferoxamine; Fer-1, ferrostatin-1; FAC, ferric ammonium citrate; SOD, superoxide dismutase; MDA, malondialdehyde; N, nucleus; M, mitochondria.

Iron overload promotes ferroptosis in PC12 cells. Pretreatment with Fer-1 or DFO was demonstrated to antagonize the reduction in cell proliferation induced by FAC (Fig. 6A). The results also demonstrated that FAC exposure significantly increased MDA and reduced SOD activity levels and induced excessive generation of ROS compared with those in control group (Fig. 6B-E). Furthermore, FAC treatment also increased the Fe^{2+} content in PC12 cells, as indicated by significantly higher FerroOrange signals compared with those observed in control cells (Fig. 6F and G). Changes in the mitochondria were also demonstrated, with FAC treatment resulting in a reduction in mitochondrial volume and increased membrane density (Fig. 6H). Furthermore, the level of lipid peroxidation assessed using confocal laser scanning microscopy demonstrated that FAC significantly increased lipid peroxidation compared with that in control cells (Fig. 6I and J). However, pretreatment with 10 μM Fer-1 and/or 100 μM DFO effectively attenuated the aforementioned damage induced by FAC treatment.

Discussion

In the present study, the results demonstrated that iron accumulation and ferroptosis occur in rats with HHIBD. DFO treatment restored the normal expression of ferroptosis-associated proteins (IRP2, FTH, TFRC, DMT1, ACSL4 and FSP1) and the levels of ferroptosis-associated biochemical markers (MDA, GSH, SOD and tissue iron).

Intraperitoneal injection of PHZ can induce hemolysis to increase the concentration of unconjugated bilirubin (25,26). Thus, compared with exogenous administration of bilirubin and Gunn rat (43,44), the PHZ-induced rat model provides a reproduction of the states of bilirubin encephalopathy secondary to hemolytic disease . According to previous data, the highest permeability of the blood-brain barrier occurs on the 10th day of life of a newborn rat pup (45). Thus, 10- to 12-day-old rats were administered PHZ and it was demonstrated that the total bilirubin level significantly increased, whereas the hemoglobin and hematocrit levels significantly decreased compared with the control group. Notably, the total bilirubin level exceeded the accepted hyperbilirubinemia threshold (>51.3 μM) in rats (26). It was also confirmed that the neonatal rats developed HHIBD by measuring the NSE and S100B levels.

Extensive research has been conducted on the potential mechanisms of bilirubin neurotoxicity *in vitro* and *in vivo*, including studies assessing oxidative stress (46), endoplasmic reticulum stress (47,48), inflammation (49), autophagy (50), apoptosis (51,52) and abnormal synthesis of both DNA and protein (53). However, the underlying mechanisms of neurotoxicity induced by bilirubin remain unclear and require further investigation. The contribution of other hemolysis products in the development of neurotoxicity have also not been well studied. Moreover, excess ferrous ion can accumulate in the basal ganglia and cause damage, and the basal ganglia is also a target site of bilirubin neurotoxicity (54).

Accumulation of peroxidized lipids is a typical characteristic of ferroptosis (55). For example, in the present study, the level of MDA was significantly increased in the PHZ group compared with the control group. Furthermore, GSH has been indicated to exhibit neuroprotective effects against bilirubin-induced cytotoxicity (56). Brain tissue GSH is reported to be significantly reduced following the induction of HHIBD in rats (26,27). Moreover, in the current study, it was demonstrated that HHIBD resulted in the downregulation of GSH levels and SOD activity and the upregulation of MDA levels. DFO, an iron-chelating agent and ferroptosis inhibitor, has been reported to induce antioxidant activity and reduce oxidative damage (57). Accordingly, pretreatment with DFO reversed the aforementioned changes. In addition, compared with the PHZ group, DFO pretreatment was demonstrated to significantly reduce the levels of NSE and S100B in the DFO + PHZ group, while the hemolysis related indicators such as hematocrit, hemoglobin and bilirubin were not alleviated. Thus, DFO pretreatment could alleviate HHIBD.

ACSL4 is considered to be a specific biomarker and driver of ferroptosis. Low expression of ACSL4 mediates glioma cell proliferation by inhibiting ferroptosis (58). In an animal model of acute brain injury, ACSL4 levels increased significantly, and knockout of ACSL4 reduced brain injury by inhibiting ferroptosis (59,60). In the present study, the expression of ACSL4 was significantly upregulated in the rat HHIBD model, which further demonstrated that ferroptosis may serve an important role in HHIBD and provides a possible intervention target for further study. Additionally, FSP1 acts as an oxidoreductase, restraining the propagation of lipid peroxides and preventing ferroptosis (61). Moreover, the expression of FSP1 was decreased in the brain tissue of rats with hemolytic hyperbilirubinemia in the present study, thereby suggesting excess lipid peroxidation in the rat model.

Another biochemical characteristic of ferroptosis is iron accumulation (62). Iron overload and an increase in lipid peroxidation products have been reported in infants with hemolytic diseases (63). These findings indicate that iron toxicity may serve a vital role in the pathobiology of severe hemolytic diseases. Results from the present study demonstrated that the level of iron was significantly elevated in the brain tissue of rats with HHIBD, which is consistent with the aforementioned studies (8,25). Intracellular iron levels are controlled by highly regulated mechanisms involving proteins, such as the iron importer TFRC, iron storage protein ferritin and FPN1 (64,65). IRP2 is the main regulator of iron metabolism and maintains intracellular iron homeostasis (66). When intracellular iron is insufficient, IRP2 can promote iron transport into cells by inhibiting the degradation of TFRC (67). TFRC is considered a positive regulator of ferroptosis, as it promotes iron intake (68,69). In the present study, it was demonstrated that iron overload caused by hemolytic hyperbilirubinemia leads to ferroptosis and serves an important role in HHIBD, based on the upregulated expression of IRP2 and TFRC in combination with the increased total iron content.

Ferritin consists of FTH and light chain subunits and is considered to be the pivotal protein for storing and dislodging excess iron to reduce cell damage and stress (64). Autophagic degradation of ferritin, mediated by lysosomes, has been reported to increase intracellular Fe^{2+} levels and promote ferroptosis (70). However, it has been reported that ferroptosis induced by iron overload is accompanied by the upregulation of FTH expression under certain pathological conditions, such as traumatic brain injury and cerebral ischemia/reperfusion injury (71). Moreover, the present study demonstrated that the level of FTH significantly increased in the PHZ group, whilst this change was restored in the DFO + PHZ group. In

summary, FTH may serve a key role in ferroptosis in HHIBD, which requires further exploration.

To further evaluate the role of ferroptosis in the neurotoxicity of iron overload, a FAC model was established *in vitro*. FAC, which has been widely used to induce iron overload, has high solubility and the ability to convert into ferrous ion (72). Typical mitochondrial features of ferroptosis include shrinking, increased membrane density and reduced or absent cristae (73,74). In the present study, ferroptosis-specific mitochondrial morphological changes in PC12 cells, induced by FAC, were demonstrated using TEM. In the FAC-induced PC12 cell damage model, Fer-1 and DFO pretreatment antagonized the increase in lipid peroxides, demonstrated using confocal laser scanning microscopy. These findings further demonstrated that iron overload could lead to neuronal damage via ferroptosis.

The present study has certain limitations. Firstly, histological analysis was not performed to visually detect the tissue damage caused by HHIBD. Secondly, recent studies have pointed out that activation of inflammation, including the activation of multiple inflammation-related signaling pathways, can lead to ferroptosis (75,76). However, plasma TNF-α, IFN-γ, IL-2 or IL-10 levels were not assessed in the animal model. In future studies, the role of inflammatory reactions in hyperbilirubinemia-induced brain damage and the interplay between inflammation and ferroptosis should be evaluated. However, higher levels of iron and MDA and lower levels of GSH and SOD activity were measured in the brain tissues of the PHZ group compared with those in the control group. In addition, HHIBD resulted in increases in the expression of the ferroptosis-related proteins ACSL4, FTH, TFRC and DMT1 and a reduction in the expression of FSP1. KEGG pathway enrichment analysis demonstrated that the differentially expressed rat brain proteins between the control and PHZ groups were significantly enriched in ferroptosis, GSH metabolism and fatty acid biosynthesis pathways. Pretreatment with DFO alleviated redox imbalance and lipid peroxidation-mediated HHIBD. PC12 cells treated with FAC showed shrinking mitochondria, high mitochondrial membrane density, and increased lipid reactive oxygen species and intracellular ferrous iron, which were antagonized by pretreatment with ferrostatin-1 or DFO.

To the best of our knowledge, this is the first study to elucidate the role of ferroptosis in HHIBD *in vivo*. The present study demonstrated the vital role of ferroptosis in HHIBD, and iron overload was demonstrated to trigger ferroptosis potentially via the activation of lipid peroxidation in the brain. These findings demonstrate that ferroptosis is involved in HHIBD and shed light on the potential underlying molecular mechanisms of HHIBD. Furthermore, the present study provides new insights into candidate proteins that are potentially involved in ferroptosis in the brain during hemolytic hyperbilirubinemia.

Acknowledgements

The authors would like to thank Professor Junjin Lin and Professor Linying Zhou (Public Technology Service Center, Fujian Medical University, Fuzhou, China) and Dr Liping Zhu, Dr Xudong Zhuang and Dr Xinrui Wang (NHC Key Laboratory of Technical Evaluation of Fertility Regulation for Non-Human Primate, Fujian Maternity and Child Health Hospital, Fuzhou, China) for their technical assistance.

Funding

The present study was supported by the Natural Science Foundation of Fujian Province (grant no. 2020J01327), the Fujian Provincial Health Technology Project (grant no. 2020GGB017), the Joint Funds for the Innovation of Science and Technology, Fujian Province (grant no. 2020Y9143), the Open Project of the Key Laboratory of Environment and Health of Fujian Medical University (grant no. GWGXZD-202002) and Fujian Maternity and Child Health Hospital (grant no. YCXM 20-08).

Availability of data and materials

Mass spectrometry proteomics data have been deposited to the ProteomeXchange Consortium (http://proteomecentral.proteomexchange.org) via the iProX partner repository with the dataset identifier PXD041604. Other datasets used and/or analyzed during the current study are available from the corresponding author on reasonable request.

Authors' contributions

HL and JZ confirm the authenticity of all the raw data. HL and LX conceived and designed the study. JZ, XL, SL, GL, JT, JL, CZ and SW performed the experiments. JZ and XL collected and analyzed the experimental data. JZ and XL prepared the first version of the manuscript. XL, SL, GL, JT, JL, CZ, SW and LX provided critical comments on the revision of the manuscript. HL and LX revised and finalized the manuscript. All authors have read and approved the final manuscript.

Ethics approval and consent to participate

The present study was approved by the Institutional Animal Care and Use Committee of Fujian Maternity and Child Health Hospital (approval no. 2020KY093; Fuzhou, China).

Patient consent for publication

Not applicable.

Competing interests

The authors declare that they have no competing interests.

References

1. Lauer BJ and Spector ND: Hyperbilirubinemia in the Newborn. Pediatr Rev 32: 341-349, 2011.
2. Soto Conti CP: Bilirubin: The toxic mechanisms of an antioxidant molecule. Arch Argent Pediatr 119: e18-e25, 2021 (In English, Spanish).
3. Christensen RD, Agarwal AM, George TI, Bhutani VK and Yaish HM: Acute neonatal bilirubin encephalopathy in the State of Utah 2009-2018. Blood Cells Mol Dis 72: 10-13, 2018.
4. Wong RJ and Stevenson DK: Neonatal hemolysis and risk of bilirubin-induced neurologic dysfunction. Semin Fetal Neonatal Med 20: 26-30, 2015.
5. Kumar V, Kumar P, Sundaram V, Munjal SK, Malhi P and Panda NK: Childhood neurodevelopmental outcomes of survivors of acute bilirubin encephalopathy: A retrospective cohort study. Early Hum Dev 158: 105380, 2021.

6. Subspecialty Group of Neonatology, Society of Pediatrics, Chinese Medical Association; Chinese Multicenter Study Coordination Group for Neonatal Bilirubin Encephalopathy: Clinical characteristics of bilirubin encephalopathy in Chinese newborn infants-a national multicenter survey. Zhonghua Er Ke Za Zhi 50: 331-335, 2012 (In Chinese).
7. Par EJ, Hughes CA and DeRico P: Neonatal Hyperbilirubinemia: Evaluation and treatment. Am Fam Physician 107: 525-534, 2023.
8. Viktorinova A: Iron-mediated oxidative cell death is a potential contributor to neuronal dysfunction induced by neonatal hemolytic hyperbilirubinemia. Arch Biochem Biophys 654: 185-193, 2018.
9. Khdair-Ahmad F, Aladily T, Khdair-Ahmad O and Badran EF: Chelation therapy for secondary neonatal iron over load: Lessons learned from rhesus hemolytic disease. Turk J Pediatr 60: 335-339, 2018.
10. Aygun C, Tekinalp G and Gurgey A: Increased Fetal iron load in rhesus hemolytic disease. Pediatr Hematol Oncol 21: 329-333, 2004.
11. Kaplan M, Bromiker R and Hammerman C: Hyperbilirubinemia, hemolysis, and increased bilirubin neurotoxicity. Semin Perinatol 38: 429-437, 2014.
12. Nishiie-Yano R, Hirayama S, Tamura M, Kanemochi T, Ueno T, Hirayama A, Hori A, Ai T, Hirose N and Miida T: Hemolysis is responsible for elevation of serum iron concentration after Regular exercises in judo athletes. Biol Trace Elem Res 197: 63-69, 2020.
13. Comporti M, Signorini C, Buonocore G and Ciccoli L: Iron release, oxidative stress and erythrocyte ageing. Free Radic Biol Med 32: 568-576, 2002.
14. Sun S, Shen J, Jiang J, Wang F and Min J: Targeting ferroptosis opens new avenues for the development of novel therapeutics. Signal Transduct Target Ther 8: 372, 2023.
15. Jiang X, Stockwell BR and Conrad M: Ferroptosis: Mechanisms, biology and role in disease. Nat Rev Mol Cell Biol 22: 266-282, 2021.
16. Ashraf A, Jeandriens J, Parkes HG and So PW: Iron dyshomeostasis, lipid peroxidation and perturbed expression of cystine/glutamate antiporter in Alzheimer's disease: Evidence of ferroptosis. Redox Biol 32: 101494, 2020.
17. Rui T, Wang H, Li Q, Cheng Y, Gao Y, Fang X, Ma X, Chen G, Gao C, Gu Z, *et al*: Deletion of ferritin H in neurons counteracts the protective effect of melatonin against traumatic brain injury-induced ferroptosis. J Pineal Res 70: e12704, 2021.
18. Vitalakumar D, Sharma A and Flora SJS: Ferroptosis: A potential therapeutic target for neurodegenerative diseases. J Biochem Mol Toxicol 35: e22830, 2021.
19. Ding X, Gao L, Han Z, Eleuteri S, Shi W, Shen Y, Song ZY, Su M, Yang Q, Qu Y, *et al*: Ferroptosis in Parkinson's disease: Molecular mechanisms and therapeutic potential. Ageing Res Rev 91: 102077, 2023.
20. Bu ZQ, Yu HY, Wang J, He X, Cui YR, Feng JC and Feng J: Emerging Role of Ferroptosis in the Pathogenesis of Ischemic Stroke: A new therapeutic target? ASN Neuro 13: 175909142110375, 2021.
21. Lu C, Tan C, Ouyang H, Chen Z, Yan Z and Zhang M: Ferroptosis in Intracerebral hemorrhage: A panoramic perspective of the metabolism, mechanism and theranostics. Aging Dis 13: 1348, 2022.
22. Li QS and Jia YJ: Ferroptosis: A critical player and potential therapeutic target in traumatic brain injury and spinal cord injury. Neural Regen Res 18: 506, 2023.
23. Ren S, Chen Y, Wang L and Wu G: Neuronal ferroptosis after intracerebral hemorrhage. Front Mol Biosci 9: 966478, 2022.
24. Luykx LM, Berger HM, Geerdink J, Kanhai HHH and Egberts J: Non-protein-bound iron and free radical damage in fetuses with rhesus haemolytic disease: Influence of intrauterine transfusions. BJOG 111: 303-310, 2004.
25. Mejia GB, Sanz CR, Avila MM, Peraza AV, Guzmán DC, Olguín HJ, Ramírez AM and Cruz EG: Experimental hemolysis model to study bilirubin encephalopathy in rat brain. J Neurosci Methods 168: 35-41, 2008.
26. Pazar A, Kolgazi M, Memisoglu A, Bahadir E, Sirvanci S, Yaman A, Yeğen BÇ and Ozek E: The neuroprotective and anti-apoptotic effects of melatonin on hemolytic hyperbilirubinemia-induced oxidative brain damage. J Pineal Res 60: 74-83, 2016.
27. Luo Y, Peng M and Wei H: Melatonin promotes brain-derived neurotrophic factor (BDNF) expression and anti-apoptotic effects in neonatal hemolytic hyperbilirubinemia via a phospholipase (PLC)-mediated mechanism. Med Sci Monit 23: 5951-5959, 2017.
28. Yao X, Zhang Y, Hao J, Duan HQ, Zhao CX, Sun C, Li B, Fan BY, Wang X, Li WX, *et al*: Deferoxamine promotes recovery of traumatic spinal cord injury by inhibiting ferroptosis. Neural Regen Res 14: 532-541, 2019.
29. Jin T, He Q, Cheng C, Li H, Liang L, Zhang G, Su C, Xiao Y, Bradley J, Peberdy MA, *et al*: UAMC-3203or/and Deferoxamine improve Post-Resuscitation myocardial dysfunction through suppressing ferroptosis in a rat model of cardiac arrest. Shock 57: 344-350, 2022.
30. Chian S, Jiang ZC, Jiang LX, Wang KT, Fan YX, Liao T, Chen WS and Yao WX: Caffeine-induced neurotoxicity mediated by Nrf2 pathway in PC12 cells and zebrafish larvae. J Appl Toxicol 42: 629-637, 2022.
31. Wiatrak B, Kubis-Kubiak A, Piwowar A and Barg E: PC12 cell line: Cell types, coating of culture vessels, differentiation and other culture conditions. Cells 9: 958, 2020.
32. Rand RN and Di Pasqua A: A new diazo method for the determination of bilirubin. Clin Chem 8: 570-578, 1962.
33. Zecha J, Satpathy S, Kanashova T, Avanessian SC, Kane MH, Clauser KR, Mertins P, Carr SA and Kuster B: TMT Labeling for the Masses: A Robust and Cost-efficient, In-solution Labeling Approach. Mol Cell Proteomics 18: 1468-1478, 2019.
34. Grebe SK and Singh RJ: LC-MS/MS in the Clinical Laboratory-Where to from here? Clin Biochem Rev 32: 5-31, 2011.
35. Men L, Li Y, Wang X, Li R, Zhang T, Meng X, Liu S, Gong X and Gou M: Protein biomarkers associated with frozen Japanese puffer fish (Takifugu rubripes) quality traits. Food Chem 327: 127002, 2020.
36. Jiang Y, Zhao J, Li R, Liu Y, Zhou L, Wang C, Lv C, Gao L and Cui D: CircLRFN5 inhibits the progression of glioblastoma via PRRX2/GCH1 mediated ferroptosis. J Exp Clin Cancer Res 41: 307, 2022.
37. Zhou Y, Li L, Mao C and Zhou D: Astragaloside IV ameliorates spinal cord injury through controlling ferroptosis in H2O2-damaged PC12 cells in vitro. Ann Transl Med 10: 1176, 2022.
38. Zuo X, Zeng H, Wang B, Yang X, He D, Wang L, Ouyang H and Yuan J: AKR1C1 Protects corneal epithelial cells against oxidative stress-mediated ferroptosis in dry eye. Invest Ophthalmol Vis Sci 63: 3, 2022.
39. Huang S, Cao B, Zhang J, Feng Y, Wang L, Chen X, Su H, Liao S, Liu J, Yan J and Liang B: Induction of ferroptosis in human nasopharyngeal cancer cells by cucurbitacin B: Molecular mechanism and therapeutic potential. Cell Death Dis 12: 237, 2021.
40. Lorimier P, Lamarcq L, Labat-Moleur F, Guillermet C, Bethier R and Stoebner P: Enhanced chemiluminescence: A high-sensitivity detection system for in situ hybridization and immunohistochemistry. J Histochem Cytochem 41: 1591-1597, 1993.
41. Jia B, Li J, Song Y and Luo C: ACSL4-Mediated ferroptosis and its potential role in central nervous system diseases and injuries. Int J Mol Sci 24: 10021, 2023.
42. Bersuker K, Hendricks JM, Li Z, Magtanong L, Ford B, Tang PH, Roberts MA, Tong B, Maimone TJ, Zoncu R, *et al*: The CoQ oxidoreductase FSP1 acts parallel to GPX4 to inhibit ferroptosis. Nature 575: 688-692, 2019.
43. Hankø E, Hansen TWR, Almaas R, Lindstad J and Rootwelt T: Bilirubin induces apoptosis and necrosis in human NT2-N Neurons. Pediatr Res 57: 179-184, 2005.
44. Shapiro SM: Somatosensory and brainstem auditory evoked potentials in the gunn rat model of acute bilirubin neurotoxicity. Pediatr Res 52: 844-849, 2002.
45. Roger C, Koziel V, Vert P and Nehlig A: Autoradiographic mapping of local cerebral permeability to bilirubin in immature rats: Effects of hyperbilirubinemia. Pediatr Res 39: 64-71, 1996.
46. Qaisiya M, Coda Zabetta CD, Bellarosa C and Tiribelli C: Bilirubin mediated oxidative stress involves antioxidant response activation via Nrf2 pathway. Cell Signal 26: 512-520, 2014.
47. Qaisiya M, Brischetto C, Jašprová J, Vitek L, Tiribelli C and Bellarosa C: Bilirubin-induced ER stress contributes to the inflammatory response and apoptosis in neuronal cells. Arch Toxicol 91: 1847-1858, 2017.
48. Schiavon E, Smalley JL, Newton S, Greig NH and Forsythe ID: Neuroinflammation and ER-stress are key mechanisms of acute bilirubin toxicity and hearing loss in a mouse model. PLoS One 13: e0201022, 2018.
49. Vodret S, Bortolussi G, Iaconcig A, Martinelli E, Tiribelli C and Muro AF: Attenuation of neuro-inflammation improves survival and neurodegeneration in a mouse model of severe neonatal hyperbilirubinemia. Brain Behav Immun 70: 166-178, 2018.
50. Qaisiya M, Mardešić P, Pastore B, Tiribelli C and Bellarosa C: The activation of autophagy protects neurons and astrocytes against bilirubin-induced cytotoxicity. Neurosci Lett 661: 96-103, 2017.
51. Shi HS, Lai K, Yin XL, Liang M, Ye HB, Shi HB, Wang LY and Yin SK: Ca2+-dependent recruitment of voltage-gated sodium channels underlies bilirubin-induced overexcitation and neurotoxicity. Cell Death Dis 10: 774, 2019.

52. Ye H, Xing Y, Zhang L, Zhang J, Jiang H, Ding D, Shi H and Yin S: Bilirubin-induced neurotoxic and ototoxic effects in rat cochlear and vestibular organotypic cultures. Neurotoxicology 71: 75-86, 2019.
53. Rawat V, Bortolussi G, Gazzin S, Tiribelli C and Muro AF: Bilirubin-induced oxidative stress leads to DNA damage in the cerebellum of hyperbilirubinemic neonatal mice and activates DNA Double-Strand break repair pathways in human cells. Oxid Med Cell Longev 2018: 1801243, 2018.
54. Youdim MB, Ben-Shachar D, Yehuda S and Riederer P: The role of iron in the basal ganglion. Adv Neurol 53: 155-162, 1990.
55. Yang WS and Stockwell BR: Ferroptosis: Death by lipid peroxidation. Trends Cell Biol 26: 165-176, 2016.
56. Al-Abdi S: Decreased glutathione S-transferase level and neonatal hyperbilirubinemia associated with Glucose-6-phosphate dehydrogenase deficiency: A perspective review. Am J Perinatol 34: 305-314, 2016.
57. Chen GH, Song CC, Pantopoulos K, Wei XL, Zheng H and Luo Z: Mitochondrial oxidative stress mediated Fe-induced ferroptosis via the NRF2-ARE pathway. Free Radic Biol Med 180: 95-107, 2022.
58. Cheng J, Fan Y, Liu B, Zhou H, Wang J and Chen Q: ACSL4 suppresses glioma cells proliferation via activating ferroptosis. Oncol Rep 43: 147-158, 2020.
59. Chen J, Yang L, Geng L, He J, Chen L, Sun Q, Zhao J and Wang X: Inhibition of Acyl-CoA synthetase long-chain family member 4 facilitates neurological recovery after stroke by regulation ferroptosis. Front Cell Neurosci 15: 632354, 2021.
60. Cui Y, Zhang Y, Zhao X, Shao L, Liu G, Sun C, Xu R and Zhang Z: ACSL4 exacerbates ischemic stroke by promoting ferroptosis-induced brain injury and neuroinflammation. Brain Behav Immun 93: 312-321, 2021.
61. Doll S, Freitas FP, Shah R, Aldrovandi M, da Silva MC, Ingold I, Goya Grocin A, Xavier da Silva TN, Panzilius E, Scheel CH, *et al*: FSP1 is a glutathione-independent ferroptosis suppressor. Nature 575: 693-698, 2019.
62. Doll S and Conrad M: Iron and ferroptosis: A still ill-defined liaison. IUBMB Life 69: 423-434, 2017.
63. Rath MEA, Smits-Wintjens VEHJ, Oepkes D, Walther FJ and Lopriore E: Iron status in infants with alloimmune haemolytic disease in the first three months of life. Vox Sang 105: 328-333, 2013.
64. Mleczko-Sanecka K and Silvestri L: Cell-type-specific insights into iron regulatory processes. Am J Hematol 96: 110-127, 2021.
65. Ganz T: New regulators of systemic iron homeostasis. Signal Transduct Target Ther 6: 280, 2021.
66. Gao G, Li J, Zhang Y and Chang YZ: Cellular iron metabolism and regulation. Adv Exp Med Biol 1173: 21-32, 2019.
67. Sfera A, Bullock K, Price A, Inderias L and Osorio C: Ferrosenescence: The iron age of neurodegeneration? Mech Ageing Dev 174: 63-75, 2018.
68. Lu Y, Yang Q, Su Y, Ji Y, Li G, Yang X, Xu L, Lu Z, Dong J, Wu Y, *et al*: MYCN mediates TFRC-dependent ferroptosis and reveals vulnerabilities in neuroblastoma. Cell Death Dis 12: 511, 2021.
69. Xiong Q, Li X, Li W, Chen G, Xiao H, Li P and Wu C: WDR45 Mutation impairs the autophagic degradation of transferrin receptor and promotes ferroptosis. Front Mol Biosci 8: 645831, 2021.
70. Zhang J, Chen X, Hong J, Tang A, Liu Y, Xie N, Nie G, Yan X and Liang M: Biochemistry of mammalian ferritins in the regulation of cellular iron homeostasis and oxidative responses. Sci China Life Sci 64: 352-362, 2021.
71. Wang P, Cui Y, Ren Q, Yan B, Zhao Y, Yu P, Gao G, Shi H, Chang S and Chang YZ: Mitochondrial ferritin attenuates cerebral ischaemia/reperfusion injury by inhibiting ferroptosis. Cell Death Dis 12: 447, 2021.
72. Liu Y, Bell BA, Song Y, Kim HJ, Sterling JK, Kim BJ, Poli M, Guo M, Zhang K, Rao A, *et al*: Intraocular iron injection induces oxidative stress followed by elements of geographic atrophy and sympathetic ophthalmia. Aging Cell 20: e13490, 2021.
73. Yang J, Zhou Y, Xie S, Wang J, Li Z, Chen L, Mao M, Chen C, Huang A, Chen Y, *et al*: Metformin induces ferroptosis by inhibiting UFMylation of SLC7A11 in breast cancer. J Exp Clin Cancer Res 40: 206, 2021.
74. Yu H, Yang C, Jian L, Guo S, Chen R, Li K, Qu F, Tao K, Fu Y, Luo F andv Liu S: Sulfasalazine-induced ferroptosis in breast cancer cells is reduced by the inhibitory effect of estrogen receptor on the transferrin receptor. Oncol Rep 42: 826-838, 2019.
75. Chen Y, Fang Z-M, Yi X, Wei X and Jiang DS: The interaction between ferroptosis and inflammatory signaling pathways. Cell Death Dis 14: 205, 2023.
76. Dou J, Liu X, Yang L, Huang D and Tan X: Ferroptosis interaction with inflammatory microenvironments: Mechanism, biology, and treatment. Biomed Pharmacother 155: 113711, 2022.

Copyright © 2023 Zhou et al. This work is licensed under a Creative Commons Attribution-NonCommercial-NoDerivatives 4.0 International (CC BY-NC-ND 4.0) License.